Nonuniform Transmission in Brain SPECT Using ^{201}Tl, ^{153}Gd, and ^{99m}Tc Static Line Sources: Anthropomorphic Dosimetry Studies and Influence on Brain Quantification

Koen Van Laere, Michel Koole, Tomi Kauppinen, Myriam Monsieurs, Luc Bouwens, and Rudi Dierck

Division of Nuclear Medicine, Ghent University Hospital, Ghent; Medical Imaging and Signal Processing Department and Laboratory for Standard Dosimetry, Ghent University, Ghent, Belgium; and Department of Clinical Physiology and Nuclear Medicine, Kuopio University Hospital, Kuopio, Finland

Nonuniform attenuation correction in brain SPECT can be done routinely by means of additional γ transmission CT (TCT) measurements, using different commercially available line-source isotopes. ^{201}Tl, ^{153}Gd, and ^{99m}Tc are among the most commonly used isotopes, depending on practical and cost-effectiveness issues. We have measured additional radiation burden from static uncollimated brain SPECT transmission sources for these isotopes. The influence of the transmission isotope on brain quantification was also measured and compared with uniform attenuation correction for phantom and human data. Full iterative transmission and emission reconstruction were compared with filtered backprojection techniques. **Methods:** Rod sources with ^{201}Tl, ^{153}Gd, and ^{99m}Tc were used on a triple-head gamma camera. Dosimetry was performed using LiF TLD-100 pellets and an anthropomorphic RANDO phantom. Effective dose equivalents were calculated on the basis of measured and extrapolated absorbed doses. For brain activity measurements, a Hoffman phantom was used. Images were corrected for scatter (triple-energy window) and were reconstructed by Chang attenuation correction and filtered backprojection as well as full iterative reconstruction (ordered-subsets expectation maximization [OSEM]). To study the effect of inhomogeneous bone attenuation, realistic measurements were performed on 10 young, healthy volunteers with ^{153}Gd TCT. After stereotactic image realignment, a volume-of-interest analysis normalized to total counts was performed. **Results:** Brain SPECT-TCT using ^{201}Tl, ^{153}Gd, and ^{99m}Tc produced total effective dose-rate equivalents of 50.3 ± 11.2, 32.0 ± 2.7, and 71.1 ± 7.1 μSv/GBq × h, respectively, representing dose equivalents of 18.6, 11.9, and 26.3 μSv for a typical 20-min brain SPECT scan at maximal used source strength. Standardized quantification resulted in insignificant differences between the isotopes and methods (Chang versus OSEM) used for nonuniform correction. Iterative reconstruction enhanced image contrast and provided more accurate gray-to-white matter ratios. Between nonuniform and uniform attenuation with an optimized attenuation coefficient, slight central discrepancies were found for volunteer studies. Significantly lower intersubject variation was found for nonuniform corrected values in infratentorial and posterior brain regions. **Conclusion:** Brain transmission scanning using ^{201}Tl, ^{153}Gd, or ^{99m}Tc results in limited effective radiation dose equivalents compared with the typical radiation burden. Relative brain perfusion quantification is not significantly different for the various nonuniform TCT isotopes. Iterative reconstruction improves gray-to-white contrasts but has no significant influence on brain perfusion semiquantification. Nonuniform attenuation correction decreases intersubject variability in the posterior brain regions that were compared, which may lead to improved sensitivity toward clinical applications.

Key Words: transmission CT; dosimetry; brain SPECT; quantification

J Nucl Med 2000; 41:2051–2062

Brain SPECT by means of additional single-photon–based transmission CT (TCT) can be done routinely with several different commercially available isotopes. The choice of TCT isotope depends primarily on practical and cost-effectiveness issues (Table 1). ^{201}Tl, ^{153}Gd, and ^{99m}Tc are among the most commonly used isotopes (*1–3*). ^{153}Gd is the transmission source of choice in most commercial systems because of its suitable physical characteristics, its relative affordability, and the possibility of measuring simultaneously ^{201}Tl, ^{99m}Tc, or ^{123}I. Isotopes such as ^{241}Am (γ energy [E_γ] = 59 keV; half-life [$t_{1/2}$] = 432 y), with a low energy and photon yield, imply high specific activities (*4*). Other isotopes such as ^{57}Co (E_γ = 122 keV; $t_{1/2}$ = 271 d), ^{109}Cd (E_γ = 88 keV; $t_{1/2}$ = 463 d), ^{195}Au (E_γ = 99 and 130 keV; $t_{1/2}$ = 183 d), and ^{123}I (E_γ = 159 keV; $t_{1/2}$ = 13 h) have appropriate energy spectra and $t_{1/2}$ but are less available, are more expensive, and in some cases overlap with frequently used ^{99m}Tc emission.

Several factors can be considered in the choice and evaluation of emission CT (ECT)–TCT isotope combinations. The two most important factors are additional radiation exposure to the patient and the capability of accurate

Received Dec. 31, 1999; revision accepted May 16, 2000.

For correspondence or reprints contact: Koen Van Laere, MD, DSc, Nuclear Medicine Division, P7, Ghent University Hospital, De Pintelaan 185, 9000 Ghent, Belgium.

TABLE 1
Physical Properties and Cost-Effectiveness of Commercial SPECT Transmission Sources

Isotope	^{201}Tl	^{153}Gd	^{99m}Tc
Half-life	73 h	240 d	6.02 h
Energy (keV)	69–81 (+167)	97 + 101	140
Physical formulation	Solution	Solid	Solution
Mode ^{99m}Tc emission	Simultaneous	Simultaneous	Simultaneous T1E2*
Mode ^{123}I emission	Sequential	Simultaneous	Sequential/simultaneous†
Typical total source strength	150–300 MBq	1–2.5 GBq	370–740 MBq
Replacements/month	10	0.06	40
Total cost/y ($) for average source strength	±4000	±6000	±700

*T1E2 = simultaneous transmission and emission.
†Simultaneous can give cross-scatter problems.

quantification of emission images, irrespective of the applied TCT isotope.

Different TCT geometries (e.g., uncollimated versus collimated) and devices exist, so there is a need for accurate dose measurements because of TCT. TCT scans can be obtained sequentially or simultaneously. In the former case, exposure of only a few minutes is necessary but there is a risk of mismatching associated with patient movement. For simultaneous TCT, the irradiation time is lengthened. Also, the quantitative information in the TCT image will be improved if appropriate cross-talk correction is performed.

Few published studies have appropriately addressed the issue of radiation burden during transmission scanning (*5*). In most cases, the authors have provided merely crude estimations on the basis of poorly described, or even inappropriate, dosimetry techniques (*6–9*).

Attenuation is one of the most important physical factors affecting SPECT quantitation (*10*). Together with compensation for other physical factors such as scatter and detector system response, it can allow generation of higher quality images for optimal clinical diagnosis and accurate estimation of radioactivity in vivo (*1*). There are two major classes of attenuation compensation methods: uniform or nonuniform. Uniform attenuation correction ([UAC] constant attenuation coefficient) can be preprocessing, intrinsic, or postprocessing. The most widely used precorrection method on commercial systems is Sorenson's method, in which correction factors are applied to projection before backprojection, on the basis of the geometric mean of the two opposing ray sums (*11*). Nonuniform Chang correction allows postreconstruction correction with factors calculated from the known attenuation distribution (*12*). This modified Chang method for nonuniform attenuation correction (NUAC) is effective and includes the attenuation distribution in the calculation of the correction factor. It is relatively fast, and overall good quantitative accuracy can be obtained in one iteration (*13*).

NUAC can also be performed by reconstruction methods that are based on iterative algorithms. The exact attenuation map through the patient can be incorporated into the projector and back-projector pair for accurate compensation. Such algorithms should give improved quantitative accuracy and decreased noise in the reconstructed image. Advances in iterative algorithms and computational speed have opened clinical perspectives for these methods, especially optimally partitioned, block-iterative methods known as ordered-subsets expectation maximization (OSEM) (*14*).

Although nonuniform corrections are evidently most important for the abdominothoracic region, the lower half of the human brain is surrounded by a complexly shaped skull base. The skull thickness influences the mean effective broad-beam attenuation coefficient by a paradoxical lowering (*15*). Although the physical importance of NUAC in SPECT imaging of highly heterogeneous sections is well recognized (*1,16,17*), the clinical relevance of NUAC for brain SPECT has been under debate. Some authors state that only modest-to-moderate improvements can be made with NUAC, but these statements have been based on receptor and absolute cerebral blood flow measurements with high uncertainties (*18,19*).

Apart for quantitation, there are other advantageous uses for brain TCT such as detection and correction of patient movement. More important, for the growing number of SPECT receptor studies in which little anatomic reference information is included in the image, TCT images may be used for coregistration or stereotactic realignment purposes, enabling improved construction of spatially standardized databases and improved anatomic correlation (*20*).

The aim of this study was twofold. First, an accurate evaluation of the additional radiation burden for brain SPECT studies using static unshielded transmission sources was performed by means of an anthropomorphic phantom. Second, the influence of the transmission isotope on relative quantification of emission brain SPECT images was measured for phantom and human perfusion studies. This outcome measure was compared with UACs. Both filtered backprojection (FBP) and full (TCT + emission) iterative reconstruction were evaluated. The relative influence of cross talk on TCT and emission scatter on semiquantification was investigated. The measurement of the relative influence of these factors and their appropriate correction was placed in the context of optimized clinical diagnostic sensitivity.

MATERIALS AND METHODS

Instrumentation

A triple-head multislice GCA-9300 camera (Toshiba; Dutoit Medical, Wommelgem, Belgium) was used with super-high–resolution lead fanbeam (SHR-FB) collimators with a focal length of 397 mm and a septal thickness of 1 mm. This configuration has a tomographic resolution of 7.8 mm at a 132-mm radius of rotation (*21*). A headrest is attached to the base of the couch at fixed height.

The external transmission source assembly is a 35-cm-long plastic tube (8-mm inside diameter, 10-mm outside diameter) filled with radioisotope in liquid or solid form (*2*). The transmission sources can be placed in the focal lines of the collimators. Rod sources filled with ^{99m}Tc (1 × 370 MBq for the ^{99m}Tc-T1E2 protocol [see below] and dosimetry study; 3 × 370 MBq for the ^{99m}Tc-T3E3 protocol), ^{201}Tl (3 × 55 MBq), and ^{153}Gd (3 × 370 MBq) were used. The latter sources are solid 4-mm diameter rods with, and are mounted inside, the plastic tubes. The fluid line sources (^{99m}Tc and ^{201}Tl) were well mixed before insertion.

For dosimetry, individually calibrated LiF Harshaw thermoluminescent dosimeters (TLD-100; 1-mm thick and 5-mm diameter; Landré-Glinderman, Vilvoorde, Belgium) were used. Calibration of the TLDs was done with ^{137}Cs (Department of Radiation Protection). Readings were performed using a Harshaw QS 3500 Reader following a standard protocol. Zero-dose calibration was done using two TLDs that remained with the measurement TLDs except in the camera room. Under the measured dose range, the SD on individual readings is <3%.

The head and neck portion (up to first rib) of the RANDO phantom (Alderson Research Laboratories Inc., Stamford, CT) consists of a human adult dried skull, filled with and surrounded by tissue-equivalent material (Alderson Research Laboratories) (Fig. 1). The phantom consisted of twelve 2-cm-thick slices. During the experiments, 14 TLDs were placed inside the 5-mm-diameter holes that are present in the RANDO phantom, covered with a paper foil and inserted between two 9.5-mm-long paraffin pellets. In this way, proper buildup and true dose measurements inside the brain volume were ensured. The complete set of measurement points is indicated on the CT image of the phantom in Figure 1.

To estimate the dose received by organs below the neck, a dose decline curve was measured on separate scans with a set of 15 uncovered TLDs placed along the axial bed axis up to a distance of 130 cm below the upper head position of the phantom. Organ doses were calculated by the combination of the phantom head and neck data with the axial TLD values through biexponential interpolation to organ position corresponding to a standard man (*22*). This approach to estimate organ doses is similar to that followed by Almeida et al. (*5*).

The values obtained from the TLD readout were corrected for ambience noise and converted in effective dose equivalent (ED) rates per source activity (in μSv/GBq × h) to compare different line sources. ED values were calculated according to recommendations of the International Commission on Radiation Protection (*23*):

$$ED(\mu Sv/GBq \times h) = \Sigma D_{T,R}(\mu Gy/Gbq \times h) \times w_R \times w_T, \quad \text{Eq. 1}$$

where w_R is the radiation weighting coefficient (one for photons

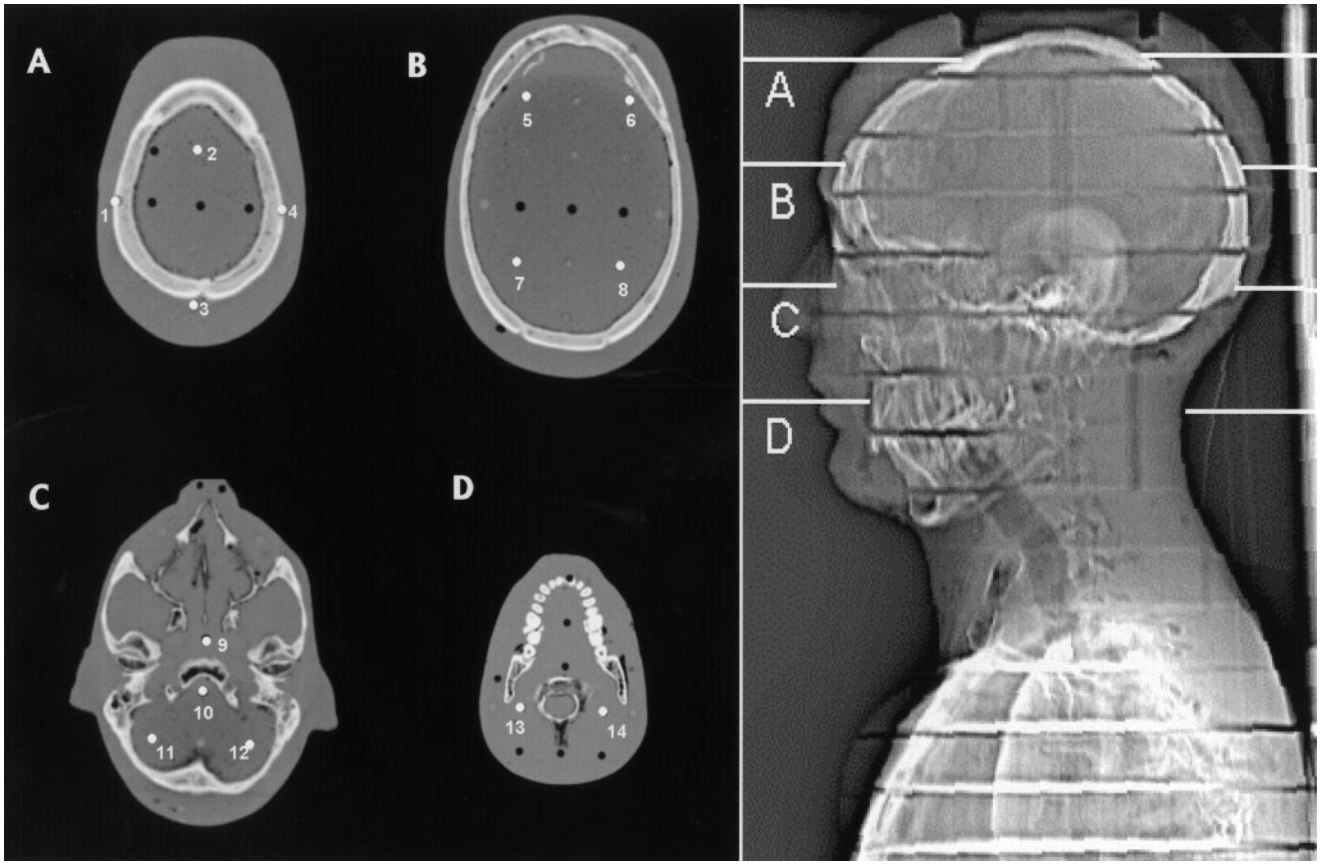

FIGURE 1. Transaxial CT scans of head and neck portion of RANDO anthropomorphic phantom with sagittal projection view. TLD dosimeter places are indicated.

and electrons), $D_{T,R}$ are the mean measured doses for each considered organ, and w_T is the weighted radiation coefficient.

A three-dimensional Hoffman brain phantom (Von Gahlen, Didam, The Netherlands) (*24*) was used to evaluate the effects of the different transmission sources on attenuation map construction, perfusion semiquantification, and effects associated with other processing parameters, as specified further. The theoretic gray-to-white contrast for this Hoffman phantom is 4:1. The phantom was carefully filled with uniformly mixed ^{99m}Tc-distilled water to which a small quantity of wetting agent was added to avoid entrapment of air bubbles. The phantom was filled with a homogeneous solution of 60 MBq ^{99m}Tc (chosen to resemble routine clinical perfusion activities: total counts acquired were typically around 4–5 million counts using SHR-FB collimation, standard 925-MBq ^{99m}Tc-ethylcysteine dimer [ECD] injections, 20-min scan).

Healthy Volunteers

^{99m}Tc-ECD SPECT studies were performed on 10 young healthy volunteers (mean age ± SD, 26.5 ± 4.5 y; age range, 21–35 y) with ^{153}Gd TCT. All subjects were screened thoroughly by history (excluding head trauma, personal neuropsychiatric history, major internal disease including diabetes mellitus, elevated cholesterol, or uncorrected hypertension) and physical examination (including neurologic and neuropsychologic examination by a skilled neurologist and psychiatrist). They all had normal high-resolution MR scans and normal biochemistry. These acquisitions were part of a larger normal dataset consisting of 90 volunteers between 20 and 80 y old. The younger age group was chosen to minimize morphological brain differences associated with aging effects. All subjects received a dose of 925 MBq ^{99m}Tc-ECD under resting conditions (eyes closed, low ambient noise level) and were scanned on average 30 min (range, 28–36 min) after injection. All volunteers gave written informed consent to the protocol approved by the ethics committee of the hospital.

Acquisition Protocols

Similar acquisitions were obtained for the Hoffman phantom and the volunteer emission scans, in continuous acquisition mode with 90 projections in a 128 × 128 matrix. Each head revolved over a double 120° rotation (where the camera revolves clockwise for the first half of the scan and counterclockwise for the second half, with on-line addition of the acquired frame counts). Scan duration was 40 s per projection angle. Fanbeam projections were converted to 128 × 128 parallel geometry data in 4° bins by the floating-point rebinning software as supplied by the manufacturer.

For ^{99m}Tc as the TCT isotope, two acquisition protocols were defined. The T1E2 protocol, in which one head measures emission and transmission simultaneously and the other two measure only emission (*25*), was compared with the T3E3 protocol, in which TCT is performed sequentially with three transmission sources before activity injection (simulated by a water-filled Hoffman phantom), after which three-head emission is measured. TCT measurements were performed over the same time period and with the same acquisition parameters when acquired sequentially for the Hoffman phantom scans.

Scatter correction for emission scans was done by means of the triple-energy window (TEW) correction method before rebinning and reconstruction (*26*). This method requires three windows for data acquisition: a main window at the photopeak and two subwindows on both sides of the main window. The primary photon count in the main window (C_{prim}) is estimated by subtracting an estimate of the scatter fraction (C_{scat}) from the total window counts (C_{total}). This scatter fraction is calculated as a linear combination of the subwindow counts:

$$C_{scat} = (C_l/W_l + C_u/W_u) \times W_m/2, \quad \text{Eq. 2}$$

where C_l and C_u are the counts in the lower and upper subwindow, and W_m, W_l, and W_u are the widths of the main window and the lower and upper subwindows, respectively.

In this study, symmetric scatter windows were set at 7% apart from the 20% window over the 140-keV peak for ^{99m}Tc. For the lower transmission energies, a 15% main window was used. To correct for ^{99m}Tc downscatter (cross talk), extra 5% scatter windows were placed adjacent to both sides of the main transmission window for simultaneous emission–transmission measurements. The same TEW approach was used for this correction. The effect of ^{99m}Tc downscatter cross talk on quantification was investigated for ^{201}Tl by comparing sequential transmission (also using the water-filled Hoffman phantom for transmission) with simultaneous ^{201}Tl transmission acquisition without scatter correction around the ^{201}Tl main window.

In all cases, the main window was filtered with a low-pass Butterworth filter of order 8 with a cutoff of 0.16 cycle per pixel and a Butterworth filter of order 8 with a cutoff of 0.08 cycle per pixel for the scatter windows (pixel size, 1.72 mm).

For the dosimetry measurements, transmission scans were acquired during 12–14 h, and appropriate correction for decay was conducted, resulting in an average source strength.

Reconstruction Procedures

For the Hoffman phantom, nonuniform attenuation maps were calculated in two ways. First, by means of a modified nonuniform Chang algorithm with one iteration (*2*), and, second, by means of iterative OSEM reconstruction (version 5.2) (*27*), with six subsets and two iterations. Blank scan data with high-count density (200 kcts per head) were acquired for all isotopes.

Theoretic energy scaling coefficients were used to adjust the narrow-beam attenuation coefficients to 140 keV. Scaling factors of 0.794 for ^{201}Tl and 0.906 for ^{153}Gd were applied (*2*,*3*). Transmission maps for human data were calculated by means of a nonuniform Chang algorithm (one iteration).

In the case of UAC, the map boundary was set at the edge of the cylindric Hoffman phantom. For volunteer data, automatic edge detection was used with a 5% contour. This value was chosen because it is coincident with the outer skull rim of the coregistered TCT images, and the latter is the optimal UAC contour (*16*). Unless stated otherwise, attenuation correction for the head support was included in the UAC calculation with a fixed μ of 0.282 per cm.

For determination of an empiric 140-keV optimal attenuation coefficient, the phantom (outer diameter, 186 mm; wall thickness, 6 mm) was filled homogeneously with water without the brain plaques inserted. Uniform attenuation maps were created by assigning a uniform value to all pixels within the emission contour (threshold, 30%). This was done for attenuation coefficients μ between 0.06 and 0.15 per cm. A similar relative optimization metric as described by Stodilka et al. (*16*) was used. Horizontal and vertical emission count profiles were determined (averaged over the central 10 pixels). These profiles were fitted quadratically to the distance (pixel position) for the width of the emission profile. A symmetric quadratic distribution was assumed given by:

$$c = c_2 \times x^2 + c_0, \quad \text{Eq. 3}$$

where c is the activity along the profile x. The coefficient c_2 will be

0 at the effective empiric attenuation coefficient μ_{eff}, thereby yielding a uniform profile. μ_{eff} was determined through quadratic interpolation from the experimental $(\mu_i, c_{2,i})$ pairs.

Emission maps were calculated by iterative OSEM (six subsets and four iterations) as well as by FBP. For the first, postfiltering with a Butterworth filter of order 8 with a cutoff of 0.4 cycle per pixel was performed; for FBP, a Shepp-Logan prefilter and a Butterworth postfilter of order 8 with a cutoff of 0.12 cycle per pixel were combined. FBP calculations were done after rebinning into parallel projections before any further processing of the data, whereas OSEM data were reconstructed directly in fanbeam mode.

Except for the OSEM data, reconstruction was performed on a Sun UltraSparc 2 (200-MHz processor, 128-MB random-access memory [RAM]; Sun Computers, Zaventem, Belgium). For iterative reconstruction, blank scan and scatter-corrected projection data were first transferred through Interfile 3.3 conversion onto a personal computer-based Hermes imaging platform under Solaris (Nuclear Diagnostics, Hägersten, Sweden). Scaling of the transmission sinogram was performed on a nonattenuated rectangular region of interest (ROI) by means of the blank scan data. Images were converted to BIGENDIAN format through an in-house conversion program (MedCon) and reconstructed on a Sun UltraSparc 10 station (300-MHz processor, 128-MB RAM; Sun Computers).

Quantification

All reconstructed images were transferred to Hermes. The reconstructed emission data were fitted automatically onto an in-house constructed perfusion database template positioned in Talaraich coordinates (*28*) that was measured with the same acquisition and reconstruction parameters as given above. The fitting procedure was performed with nine parameters (scale, shift, and rotation) using a principal axis transform and a count-density minimization algorithm (fit threshold, 0.50: BRASS Brain Registration and SPECT Semiquantification; Nuclear Diagnostics). On this template, a predefined set of 19 volumes of interest (VOIs) was determined, which was used for semiquantification, as published (*29*). VOI data were grouped according to the following classification along their attenuation characteristics: 1, cortical; 2, subcortical (basal ganglia, mesiotemporal); 3, central (thalamus); and 4, subtentorial (cerebellum and pons). Gray-to-white ratios were determined on two consecutive slices 35 mm above the anterior commissure–posterior commissure plane by small square ROIs (3×3 pixels; pixel size, 3.59 mm) that were placed in a ventricular-free white matter area and centrally in the cortex. These small ROIs were taken to exclude partial-volume effects as much as possible.

Statistics

Nonlinear curve-fitting parameters and all statistics were calculated with SPSS (version 7.5 for Windows; SPSS Inc., Heverlee, Belgium). The Friedman test was used to detect significant differences between reconstruction procedures for subtentorial, subcortical, central, and cortical brain VOI data. The Wilcoxon signed rank test, which considers both direction and size of differences, was used to analyze paired semiquantitative results.

RESULTS

Dosimetry

The dose rate per unit source strength, averaged over the head of the RANDO phantom, was 203 ± 45, 129 ± 11, and 255 ± 25 μGy/GBq × h for ^{201}Tl, ^{153}Gd, and ^{99m}Tc, respectively. Figure 2 shows the measured stray radiation

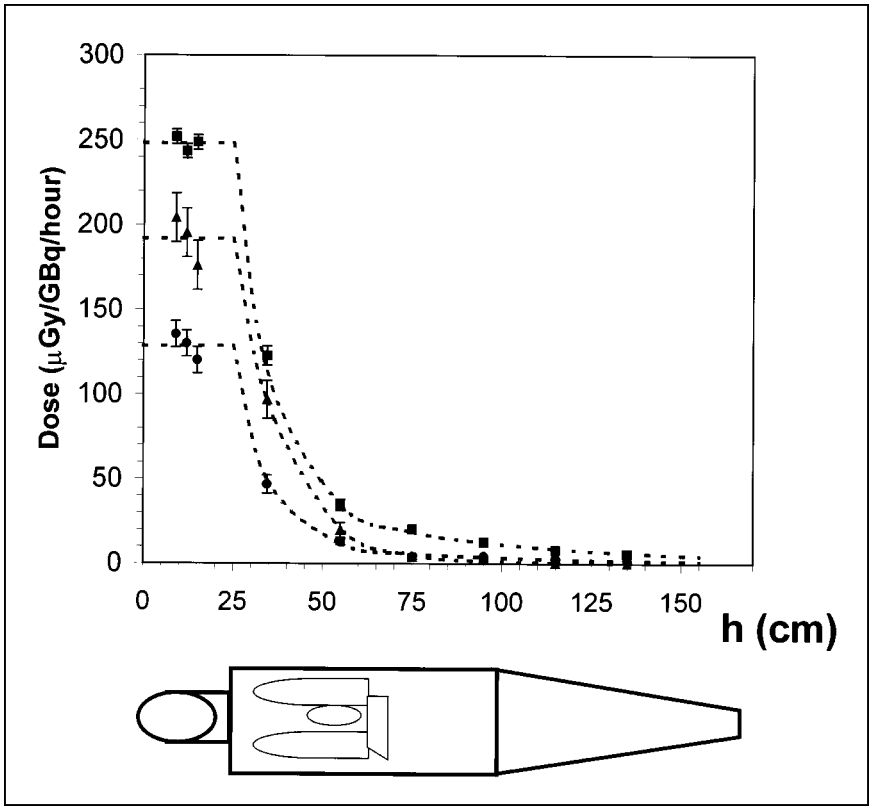

FIGURE 2. Stray scatter profile along bed axis measured by open thermoluminescent dosimeters for ^{201}Tl (▲), ^{153}Gd (●), and ^{99m}Tc (■) line sources in gamma camera. Constant value in field of view is assumed. Biexponential fits are given (dashed lines). Dose rate values are normalized to unit source strength. A reference man is schematized along horizontal axis.

profile along the central axis of the patient bed for all three TCT isotopes used. This axial profile measured with unshielded TLD pellets was used for calculation of target organ doses below the neck. A very rapid decline is noted from the upper thorax position onward. The fast distance-decay constants of the biexponential fit through these data were 0.08 ± 0.01, 0.11 ± 0.01, and 0.10 ± 0.01 per cm (estimate ± asymptomatic SE) for ^{201}Tl, ^{153}Gd, and ^{99m}Tc measurements, respectively. This indicates a similar relative dose decline rate with axial distance, which is slightly lower for ^{201}Tl. This is probably associated with an increased scatter component at lower photon energy.

Effective dose equivalents were calculated for the different isotopes and expressed as effective dose equivalent rate per unit source activity (μSv/GBq × h). These results are given in Table 2 for the different target organs and total body. Converted to the maximal source strength at the time of preparation or purchase, the average effective dose equivalents (±SD) for a typical 20-min scan duration were 18.6 ± 4.2, 11.9 ± 1.0, and 26.3 ± 2.6 μSv for ^{201}Tl, ^{153}Gd, and ^{99m}Tc, respectively.

Homogeneous Phantom Measurements

Calculated narrow-beam attenuation coefficients for Chang reconstructed attenuation maps were $\mu_{^{201}Tl} = 0.189 \pm 0.012$, $\mu_{^{153}Gd} = 0.178 \pm 0.006$, and $\mu_{^{99m}Tc} = 0.155 \pm 0.005$ per cm (value for water at the isotope energy $E_\gamma \pm 1$ SD). These values are in good agreement with theoretic narrow-beam linear attenuation coefficients of $\mu_{th,^{201}Tl} = 0.187$, $\mu_{th,^{153}Gd} = 0.175$, and $\mu_{th,^{99m}Tc} = 0.154$ per cm (*2,30,31*).

For attenuation coefficients ranging from 0.06 to 0.15 per cm, uniform Sorenson attenuation maps were created. From the μ-axis intercept of the quadratic fit through the plot of experimental $(\mu_i, c_{2,i})$ values, an optimal value of $\mu_{eff} = 0.105 \pm 0.004$ per cm was found for the empiric broad-beam attenuation coefficient.

TABLE 2
Calculation of Equivalent Dose Rate and Effective Dose Equivalent (ED) Rate (±SD) for Three Line Sources of Toshiba GCA9300 Gamma Camera

Organ	μSv/GBq × h		
	^{201}Tl	^{153}Gd	^{99m}Tc
Gonads (testes)	0.2	0.7	2.3
Bone marrow	6.2	3.8	8.5
Colon	0.8	0.8	2.5
Lung	5.6	2.7	7.2
Stomach	1.7	1.1	3.4
Bladder	0.1	0.2	0.5
Breast	1.7	0.9	2.4
Liver	0.7	0.5	1.4
Esophagus	3.2	1.5	3.9
Thyroid	9.6	6.4	12.4
Skin	0.3	0.2	0.5
Bone surface	0.5	0.3	0.7
Other	19.5	13.0	25.4
ED (μSv/GBq × h)	50.3 ± 11.2	32.0 ± 2.7	71.1 ± 7.1

Hoffman Phantom Measurements

Semiquantitative values for the Hoffman phantom, obtained with the different nonuniform transmission maps, were calculated and are given in Table 3. Figure 3 shows a box plot for the semiquantification for the regional subgroups as defined above. There were no significant differences between either group (subgroup Friedman test; $P > 0.10$). The total FBP reconstruction time for scatter correction, Chang transmission, and corrected emission was on average 10 min.

Between the different TCT isotopes used, no significant differences were found for the emission values calculated with OSEM combined transmission and emission (Friedman test for all subgroups; $P = 0.08$–0.41). There were also no significant differences for the subgroups between fully iteratively reconstructed semiquantified images and FBP images with Chang NUAC ($P = 0.28$–0.70). The time for total (emission + transmission) iterative reconstruction was on average 8 min.

When studying effects of simultaneous versus sequential transmission for ^{99m}Tc measurements, there were no significant differences for all subgroups for semiquantitative outcome values for the T1E2 and T3E3 acquisition protocol (Friedman test; $P > 0.20$) (values also included in Table 3 and subregions shown in Fig. 3).

To evaluate the effects of correction for scatter and emission–transmission cross talk, the ^{201}Tl transmission scans were reconstructed with and without ^{99m}Tc downscatter cross talk, corrected by TEW. This resulted in highly significant differences for the subcortical (99.1 versus 90.0; Wilcoxon $P = 0.003$) and central brain (100.5 versus 86.4; Wilcoxon $P = 0.001$) regions. Ignoring cross talk provides falsely high contributions of scattered ^{99m}Tc photons in the thallium projection data. This scatter fraction is maximal at the center of the object and will therefore lead to an underestimation of central attenuation coefficients.

Emission scatter correction had a relatively smaller influence on quantification values, as can be seen from Table 3, where this comparison is included for ^{99m}Tc-T1E2 measurements. However, for the subregions, a significant difference was found in the subcortical regions (95.5 versus 100.9; Wilcoxon $P = 0.001$), most likely caused by the inward scatter of cortical activity. Central region differences did not reach statistical significance (93.1 versus 99.1; Wilcoxon $P = 0.12$), which may be, in part, associated with the fact that the thalamic activity is less influenced by spilling activity of the surrounding brain.

Uniform phantom reconstruction was conducted with and without inclusion of theoretic attenuation of the head holder (Table 3). UAC without head support modeling resulted in 1.8% lower cerebellar and 1.5% lower occipital relative uptake values.

The optimized value of $\mu_{eff} = 0.105$ was used to compare emission on the basis of the nonuniform attenuation maps obtained with the ^{99m}Tc-E3T3 protocol and with uniform

TABLE 3
Contrast and Semiquantitative Results for UAC and NUAC Methods with Three Different Transmission Isotopes

Transmission isotope		^{99m}Tc-T3E3	^{99m}Tc-T1E2	^{99m}Tc-T1E2	^{201}Tl	^{201}Tl	^{153}Gd	—	—	^{99m}Tc-T3E3	^{201}Tl	^{153}Gd
Emission		FBP Chang*	FBP Chang	FBP Chang	FBP Chang	FBP Chang	FBP Chang	FBP Sorenson†	FBP Sorenson + head support	OSEM OSEM	OSEM OSEM	OSEM OSEM
Transmission												
TEW scatter correction		Yes	Yes	No E scatter	Yes	No T scatter	Yes	Yes	Yes	Yes	Yes	Yes
Contrast (gray:white)		3.66	3.28	2.28	3.63	3.38	3.58	3.01	3.12	3.79	3.61	3.89
VOI‡	VOI size§											
Cortex												
Frontal L	1483	100.2	94.8	93.6	100.5	102.9	98.6	102.4	98.3	104.2	104.6	98.8
Frontal R	1517	102.6	103.9	101.7	108.5	112.2	106.8	117.1	113.8	107.5	106.1	106.3
Temporal L	593	108.3	106.6	105.0	107.5	108.2	103.8	98.1	98.4	106.6	104.5	110.9
Temporal R	592	109.4	111.7	109.1	107.3	106.4	110.2	102.5	104.5	100.5	108.4	102.7
Sensorimotor L	254	106.0	99.2	100.4	102.6	101.2	101.9	89.3	88.5	101.4	110.0	111.3
Sensorimotor R	260	110.9	112.8	111.8	106.7	105.4	113.7	106.5	106.5	107.5	118.5	110.1
Parietal L	425	105.1	101.5	100.6	100.0	100.4	102.5	95.4	96.0	101.5	102.2	103.9
Parietal R	425	105.3	105.4	104.7	98.3	98.2	113.4	98.7	99.2	100.5	107.8	102.4
Occipital L	591	94.6	94.2	94.4	91.4	94.2	97.3	96.3	98.6	97.9	95.0	95.2
Occipital R	576	88.5	87.6	89.6	84.7	87.1	89.5	86.8	87.6	87.9	86.2	86.4
Subcortical												
Mediotemporal L	177	87.6	93.2	97.7	87.3	80.8	85.0	86.7	90.1	94.8	84.5	90.3
Mediotemporal R	166	91.1	84.5	90.9	94.2	84.8	92.7	83.0	87.1	82.9	94.3	85.6
Striatal L	181	101.5	103.4	108.1	105.5	96.2	98.9	102.4	106.9	103	100.5	104.7
Striatal R	176	106.3	108.3	112.1	109.5	98.0	103.1	106.7	112.6	104	106.1	111.3
Central												
Thalamus L	118	92.1	87.2	95.0	90.4	76.5	87.0	85.3	91.2	85.8	82.3	96.5
Thalamus R	114	88.3	82.5	91.3	96.0	81.0	85.0	83.0	89.5	89	86.1	87.9
Pons	130	103.6	109.6	111.0	115.3	101.8	109.0	95.6	98.0	104	103.6	113.9
Cerebellum												
Cerebellum L	829	93.9	95.3	97.4	95.4	95.8	88.9	95.9	97.9	97.5	93.2	96.7
Cerebellum R	767	92.1	93.0	93.5	91.9	91.4	95.2	93.1	94.5	89.2	90.0	93.3

*Iterative Chang, one iteration.
†μ_{eff} = 0.105 per cm; $\mu_{head\ holder}$ = 0.282 per cm.
‡Normalization to total VOI counts.
§In voxels of 3.59 × 3.59 × 3.59 mm^3.
T3E3 = sequential transmission and emission on all three camera heads; T1E2 = simultaneous transmission and emission; E = emission; T = transmission.

attenuation. No significant relative uptake differences were found between nonuniform and uniform attenuation for the above described subregions (Friedman test; P = 0.11–0.47).

Contrast Recovery

The theoretic gray-to-white matter activity ratio for the Hoffman phantom is 4:1. For both NUAC FBP and OSEM reconstruction with the various TCT isotopes as well as for UAC, the measured gray-to-white ratios are also included in Table 3. Contrast recovery was good for FPB NUAC but still slightly better for iterative reconstruction (ratios, 3.62 versus 3.76). Both methods of NUAC improved contrast with respect to UAC (ratio, 3.12). No scatter correction on the emission data (^{99m}Tc-T1E2) reduced contrast severely to an activity ratio of 2.28.

Nonuniform Versus Uniform Attenuation for ^{99m}Tc-ECD in Healthy Volunteers

Measured attenuation coefficients for human brain tissue after linear energy scaling to 140 keV were 0.153 ± 0.007, which is in good agreement with true narrow-beam values of 0.159 for brain tissue and 0.254 ± 0.014 for bone (skull) compared with the theoretic value of 0.246 per cm (*31*).

Figure 4 shows an example of ^{99m}Tc-ECD perfusion scans of a healthy volunteer with uniform and nonuniform ^{153}Gd transmission.

The results of the semiquantification with normalization to the total VOI counts for nonuniform ^{153}Gd transmission (iterative Chang transmission and FBP emission) (NUAC) and Sorenson uniform attenuation with μ_{eff} = 0.105 are

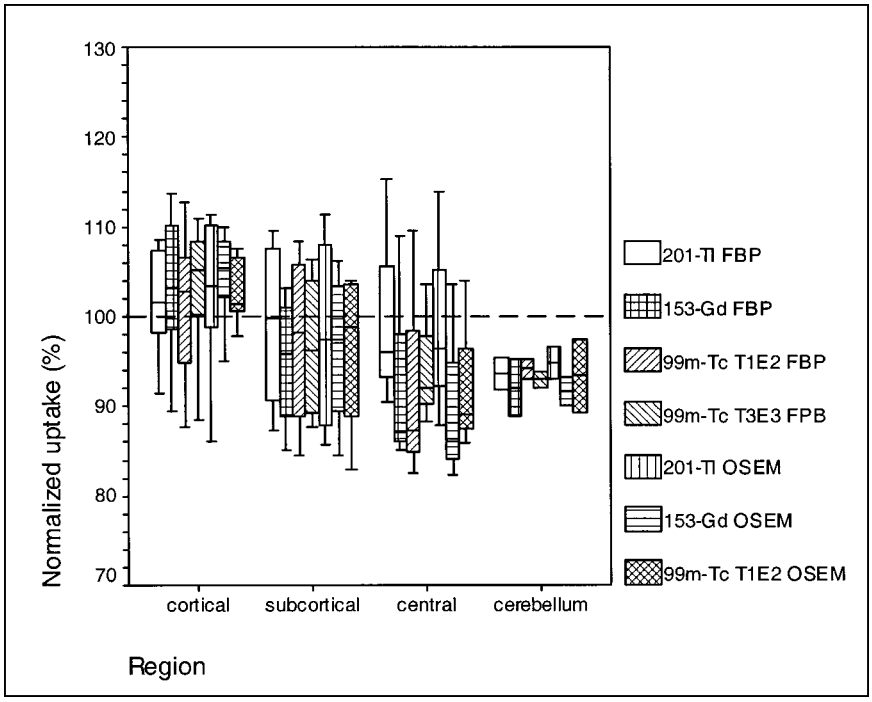

FIGURE 3. Box-and-whisker plot for Hoffman phantom activity semiquantification obtained in cerebellar, cortical, subcortical, and central regions for isotopes ^{201}Tl, ^{153}Gd, and ^{99m}Tc. Iterative (OSEM) and FBP reconstruction techniques are compared. For ^{99m}Tc FBP, simultaneous ECT–TCT (T1E2) was also compared with sequential ECT–TCT (T3E3).

given in Table 4. Significant differences were found for the cerebellum, subcortical, and central values. For the pons, differences of −1.7% were present (Wilcoxon $P = 0.29$; not significant); for all cortical regions, no significant changes were found (Wilcoxon $P = 0.26$–0.94). The radial gradient present in the supratentorial regions indicates that a lower effective attenuation coefficient for UAC may have been appropriate to match NUAC values more closely.

Interestingly, in this series a significantly smaller SD on the relative uptake values was found for the subtentorial region and occipital cortex (4.2 versus 6.7; Wilcoxon $P = 0.04$). The influence of irregular skull or head support (or both) is largest in these regions. The relative uptake values were not significantly different for the other regions (4.7 versus 4.6; $P = 0.7$).

DISCUSSION

Transmission scanning poses an extra radiation burden to the patient and, therefore, needs be evaluated carefully. Several transmission imaging geometries have been proposed, but for brain imaging line sources in the focal line of fanbeam collimators are most widely used (*1*,*32*). The combination of a line-source and fanbeam collimator has the advantages of small scatter photon fraction, relatively lower dose content of the TCT source, and easy handling.

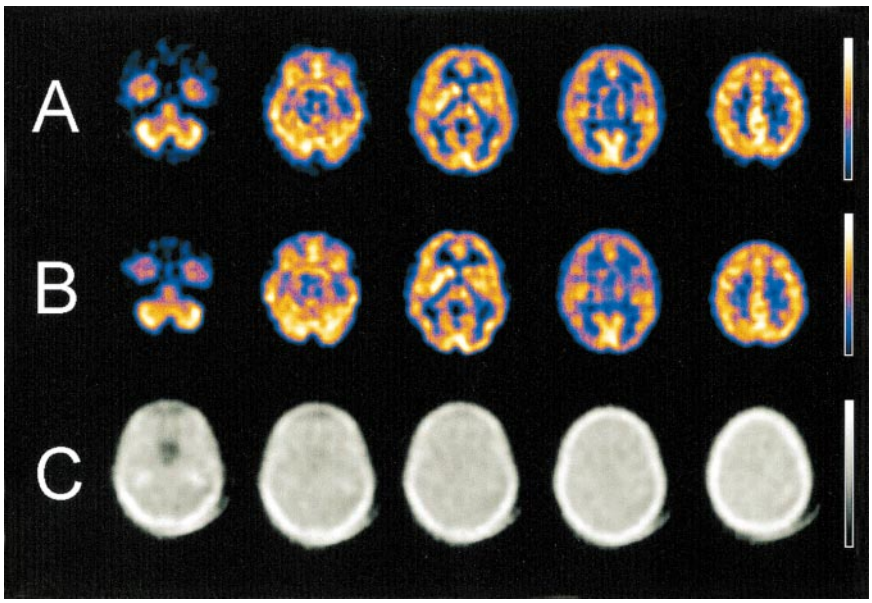

FIGURE 4. ^{99m}Tc-ECD perfusion scans for healthy volunteers with nonuniform (A) versus uniform transmission (B) at different levels parallel to commissural plane. (C) ^{153}Gd transmission CT map.

TABLE 4
Semiquantification of ^{99m}Tc-ECD Perfusion Studies for 10 Healthy Volunteers with Nonuniform Versus Uniform Transmission Correction

Region	VOI size*	NUAC† (^{153}Gd)	UAC‡	Difference	*P*§ (*t* test)
Cortical					
Frontal	3000	97.1 ± 1.7	97.7 ± 3.6	−0.6	(0.53)
Sensorimotor cortex	514	98.6 ± 4.6	98.7 ± 5.0	−0.1	(0.94)
Temporal	1185	93.2 ± 2.7	92.7 ± 2.4	0.6	(0.49)
Parietal	850	99.5 ± 3.3	100.3 ± 3.4	−0.9	(0.26)
Occipital	1167	100.9 ± 2.2	99.8 ± 6.2	1.1	(0.54)
Total	6716	97.5 ± 1.6	97.6 ± 1.6	−0.1	(0.78)
Subcortical					
Mediotemporal	343	70.7 ± 3.8	74.3 ± 3.8	−3.7	0.006
Basal ganglia	357	111.0 ± 4.9	117.4 ± 4.7	−6.4	0.001
Total	700	91.1 ± 3.6	96.2 ± 3.0	−5.1	0.000
Central					
Thalamus	232	94.3 ± 4.8	100.9 ± 4.6	−6.7	0.000
Pons	130	82.9 ± 4.9	84.2 ± 6.0	−1.3	(0.29)
Total	362	90.2 ± 3.0	94.9 ± 3.1	−4.8	0.000
Cerebellum	1596	116.7 ± 5.1	113.0 ± 6.1	3.7	0.023

*In voxels of 3.59 × 3.59 × 3.59 mm^3.
†NUAC with ^{153}Gd and iterative Chang (one iteration); semiquantitative values are given in % ± SD with normalization to total VOI counts.
‡Uniform Sorenson attenuation correction ± SD with $\mu_{eff} = 0.105$ per cm.
§Values in parentheses are not significant.

Note from our measurements that the effective radiation dose equivalent from static line sources in brain SPECT accounts for <1% of the total average patient radiation burden. Our dose calculations were based on conservative estimates for body regions lower than the neck, because it was assumed that relevant organs received the (overestimated) midsagittal plane surface dose. The everyday use of ^{99m}Tc and ^{201}Tl TCT sources implies even lower patient doses because the values given here were calculated at the initial maximal source strength, which will decline, depending on the time interval after source loading and the source changing time interval.

Relatively, ^{99m}Tc was found to produce the highest effective dose equivalent, primarily associated with the higher radiation dose for body organs below the neck. Therefore, decreasing stray radiation by means of extra shielding toward the scanner bed or use of collimated line sources is expected to produce a significantly lower radiation burden. We had also performed measurements for our department's Prism 3000 camera (Picker International, Cleveland, OH), where dose rates of only 2.0 ± 0.4 μSv/GBq × h were measured for a 2.2-GBq shielded and collimated single line source, under the same conditions and with the same head phantom (K. Van Laere, unpublished data, October 1999).

Only a few published studies have addressed the dosimetric implications of TCT in SPECT. The use of anthropomorphic phantoms was included in only one study, in which a realistic contribution of attenuation and scatter is considered as are build-up effects associated with the localization of the dosimeters inside the body (*5*). These authors measured dose equivalents for a dual-head camera with two 4-GBq ^{153}Gd scanning linear sources and a similar anthropomorphic phantom including the thorax. They measured typical brain SPECT doses of 5.8 ± 2.6 μSv, which is two to five times smaller than the doses in this work with an uncollimated unshielded configuration.

In most other studies, the authors provided values for maximum absorbed dose measured at the skin surface and did not estimate the effective dose equivalent value, which is the true biologic measure of patient radiation burden. Murase et al. (*6*) found additional patient radiation dose equivalent rates of 750 μGy/GBq × h for an unshielded 185-MBq flood source of ^{99m}Tc. Ficaro et al. (*4*) merely estimated doses with a survey meter and stated approximate values for a 2- to 20-min scan of 30 μGy/GBq for a 5.55-GBq ^{241}Am source and 810 μGy/GBq for a 444-MBq ^{99m}Tc source. Kluge et al. (*7*) found values for cardiac scanning line sources of <3 μSv/GBq × h, but their measurement method was not specified. Prvulovich et al. (*9*) measured rates of <7.6 μSv/GBq × h for 7400-MBq transmission scans with two collimated line sources. Hashimoto et al. (*8*) measured absorbed dose by TLD during a 15-min transmission scan with 3 × 370-MBq ^{99m}Tc, using blank BeO dosimeters on the edge of a brain phantom, thereby estimating skin doses. They reported very high effective dose equivalent rates of 790 μSv/GBq × h. Although some large variations in dose rate exist between the different approaches, in most cases the extra radiation burden is comparably low. It is clear that collimated and

shielded line sources can substantially reduce additional patient (and staff) radiation burden.

For the SPECT measurements, the validity of TEW correction has been shown by Monte Carlo calculations (*33*). TEW correction compensates for both the self-scattering and the cross talk between lower energy isotopes and ^{99m}Tc (*34*). Other methods for scatter correction have been applied in clinical situations (*19*) and have shown that images with triple-energy correction can be noisier. Therefore, prefiltering of the projection data before reconstruction was performed. Although it has been stated that narrow-beam attenuation coefficients should be used when applying attenuation correction that has been corrected for scatter (*30*), we have found lower values to be appropriate for reconstruction of a uniform emission density with Sorenson attenuation correction. This finding indicates that optimization of attenuation coefficients, depending on various amounts of scatter in the images, is not straightforward. Although spectral scatter correction methods such as TEW are relatively easy to implement, it is only a first-order approximation toward true scatter correction, and a significant number of scattered photons may still be present in the projection data. Our findings are in accordance with those by Stodilka et al. (*35*), who showed for several different scatter corrections (including optimal patient-dependent scatter correction) that the use of narrow-beam attenuation coefficients for scatter-corrected UAC might not be justified. The issue of optimal attenuation coefficients is further complicated by skull presence, which requires an additional reduced broad-beam attenuation coefficient (*35*).

Nonuniform correction using the Chang first-order algorithm may not be optimal for attenuation correction and, for better accuracy, nonuniform attenuation may be needed as an integral part of iterative algorithms. However, our phantom experiments have shown that nonsignificant differences in emission reconstruction semiquantification result using an iterative versus the Chang first-order scheme. Also, Dey et al. (*36*) have shown that, for cardiac studies, Chang versus OSEM are quantitatively equivalent with comparable calculation times.

Also, simultaneous versus sequential transmission with ^{99m}Tc resulted in nonsignificant differences. This fact proves an appropriate separation of emission and transmission data for the simultaneous T1E2 protocol and allows its practical use in routine applications because sequential T3E3 scanning is impractical for brain studies with delayed scanning after injection.

For the correction of attenuation maps to the emission energy at 140 keV, linear scaling of attenuation coefficients was used. Because for relatively high-Z elements, such as calcium in bone, the photoelectric probability increases proportionally with Z^4 and E^{-3}, linear scaling may not be sufficient for tissues containing heavier elements and the use of single-value scaling factors is only approximate (*3,4*). One possible way to evaluate this, using measured TCT maps, is by image coregistration of the transmission images, which allows establishment of a functional relationship between the different isotope attenuation coefficients by generation of a two-dimensional histogram of individual voxel values that can be related by least-square fitting (*18*). This approach was not attempted because human data, including skull, were available with only single TCT isotope data.

Contrast enhancement between gray and white matter is influenced by scatter correction and attenuation. From our measurements, scatter correction produced only modest changes in semiquantitative values, in contrast to changes of 20%–30% for absolute quantitative ^{123}I-iodoamphetamine (IMP) data as measured by Iida et al. (*19*). They found that neocortical and subtentorial regions were underestimated, whereas white matter tended to be overestimated without scatter correction. Because of the semiquantitative approach, the underestimation for the neocortical regions is similar. Hence, differences after semiquantification were noted only for the subcortical regions. However, white matter was also overestimated more without scatter correction, in agreement with previous findings. Similar contrast measurements for the same Hoffman phantom reconstructed without scatter and attenuation correction resulted in a ratio of 1.70 for the same camera (*21*).

The narrow-beam attenuation coefficient for 140-keV photons in water is 0.15 per cm, whereas the broad-beam coefficient appropriate for most imaging geometries had been stated as ~0.10–0.12 per cm (*37*). However, the value of $\mu_{eff} = 0.105$ per cm, which was found to be optimal for the Hoffman phantom, may not be simply transformed to an optimal coefficient for realistic human data. Slight differences (of the order 6%), predominantly central and subcortical, were present between NUAC and UAC. Stodilka et al. (*16*) has shown that the attenuating effect caused by bone makes peripheral quantification difficult, particularly adjacent to regions of thick bone. The optimal coefficient used in UAC is dependent on skull thickness and, therefore, may also be slice dependent. For ideal relative quantification, smaller values of μ are needed to correct for attenuation in a cerebellar slice than in cortical slices.

From the clinical point of view, different conclusions have been reached by authors who reviewed or investigated the importance of NUAC for the brain. Rajeevan et al. (*18*) reported that only moderate improvements in the measurement of absolute activity in individual brain ROIs were present for dopamine-transporter studies. Semiquantitative measurements of target-to-background ratios showed only small differences compared with UAC or even no attenuation correction. This statement was based on measurements with high coefficients of variation (up to 30%); nevertheless, large individual and group differences were found compared with SDs, but no additional statistics were performed. Iida et al. (*19*) stated that loss of accuracy was small when constant uniform attenuation maps were compared with measured attenuation coefficients. Again, no statistical measures were expressed to determine whether the differences were signifi-

cant. For the absolute IMP perfusion data in this work, coefficients of variation on the regional cerebral blood flow (rCBF) values are of the order 15%–20%. This is in contrast to the more sensitive semiquantitative values with coefficients of variation of the order 5%–8%.

When accurately quantified cerebellar uptake values are of importance, certainly when assumptions on stability of reference regions (e.g., cerebellum) are made, NUAC may be important. Anatomically, the assumption of uniform attenuation in the head remains questionable, because skull, sinus cavities, and head holder have attenuation properties different from those of brain tissue; other authors have shown that the assumption of homogeneous attenuation throughout the head can result in large quantitative errors (*38*). This is also in agreement with Licho et al. (*39*), who found significant differences in clinical brain SPECT count profiles depending on how attenuation compensation was made. These authors concluded that cerebellar uptake needs to be measured by NUAC. Stodilka et al. (*16*) also showed that NUAC must be performed to accurately estimate relative rCBF, especially the cerebellar count estimate. This study has also shown quantitatively that the magnitude of errors associated with UAC is comparable or greater than the uncertainties associated with intersubject variability and, therefore, than clinically demonstrable effects.

Moreover, appropriate NUAC may reduce intersubject variability for normal datasets. In our series, significantly smaller relative uptake SDs were found for the subtentorial region and occipital cortex. The effects were largest in the cerebellum and occipital cortex, probably associated with inhomogeneous surrounding skull and improved head holder correction. These findings are in accordance with the expectation of Licho et al. (*39*) and Ogasawara et al. (*34*) and may indicate that NUA-corrected control databases can provide information regarding the normal range of cerebral activity versus cerebellar activity that is at least not influenced by anatomy. Therefore, NUAC can also improve accuracy and statistical strength in interpretation of clinical studies. Quantitative comparison of relative data between nuclear medicine facilities may be more feasible and diminish variability between clinical reports. This issue must be addressed further for larger data sets of healthy volunteers of different ages.

We have evaluated the use of three line sources for brain transmission scanning with respect to quantitation, but the results are directly extendable to other sources in the same energy range. Apart from quantitation, there are other uses for transmission data. These include motion detection and correction, definition of anatomic ROI and spatial coregistration through the construction of three-dimensional reference skull data for more accurate localization, and inter- or intramodality coregistration of anatomically ill-defined ligand studies (e.g., receptor) (*1*,*40*). Apart from single-photon ECT–TCT systems, combined high-resolution x-ray transmission CT and SPECT systems may offer an alternative solution, with the added advantage of detailed patient anatomy (*40*). Although technical issues in detector optimization need to be addressed further, clinical applications of such devices may include evaluation of head trauma and stroke. These applications were out of the scope of this work but further stress the importance of nonuniform TCT in clinical and research brain SPECT.

CONCLUSION

Effective dose equivalent values derived from TCT scans are comparable with values mentioned in the literature for similar sources and geometries and add $<1\%$ to the radiation burden in a typical perfusion or receptor nuclear medicine brain SPECT scan. Therefore, radiation burden is not limiting to the use of transmission measurements in clinical brain SPECT. The choice of the transmission isotope does not influence the NUAC significantly. Compared with FBP, iterative reconstruction (OSEM) allows reconstruction of the highest gray-to-white ratios but does not improve semiquantification. Transmission imaging can decrease intersubject variability in posterior cerebral and subtentorial regions and may allow more sensitive diagnostic applications.

ACKNOWLEDGMENTS

The authors thank Erik Nolf, engineer, for the use of his image format-conversion software MedCon and the Radiotherapy Department for the use of the RANDO phantom. The authors gratefully acknowledge the support by Ivan Verbruggen (Dutoit Medical) and the logistical support obtained from Nuclear Diagnostics and Sun Computers. This research was supported by a research grant of Ghent University, a Special Research Grant of the Flemish Government (BOZF 01104699), and Het Vlaamse Instituut voor de Bevordering van het Wetenschappelijk Technologisch Onderzoek in de Industrie.

REFERENCES

1. Bailey DL. Transmission scanning in emission tomography. *Eur J Nucl Med.* 1998;25:774–787.
2. Ichihara T, Motomura N, Ogawa K, Hasegawa H, Hashimoto J, Kubo A. Evaluation of SPET quantification of simultaneous emission and transmission imaging of the brain using a multidetector SPET system with the TEW scatter compensation method and fan-beam collimation. *Eur J Nucl Med.* 1996;23:1292–1299.
3. Welch A, Gullberg GT, Christian PE, Datz FL. A comparison of Gd/Tc versus Tc/Tl simultaneous transmission and emission imaging using both single and triple detector fan-beam SPECT systems. *IEEE Trans Nucl Sci.* 1994;41:2779–2786.
4. Ficaro EP, Fessler JA, Rogers WL, Schwaiger M. Comparison of americium-241 and technetium-99m as transmission sources for attenuation correction of thallium-201 SPECT imaging of the heart. *J Nucl Med.* 1994;35:652–663.
5. Almeida P, Bendriem B, de Dreuille O, Peltier A, Perrot C, Brulon V. Dosimetry of transmission measurements in nuclear medicine: a study using anthropomorphic phantoms and thermoluminescent dosimeters. *Eur J Nucl Med.* 1998;25:1435–1441.
6. Murase K, Tanada S, Inoue T, Sugawara Y, Hamamoto K. Improvement of brain single photon emission tomography (SPET) using transmission data acquisition in a four-head SPET scanner. *Eur J Nucl Med.* 1993;20:32–38.
7. Kluge R, Sattler B, Seese A, Knapp WH. Attenuation correction by simultaneous emission-transmission myocardial single-photon emission tomography using a

technetium-99m-labelled radiotracer: impact on diagnostic accuracy. *Eur J Nucl Med.* 1997;24:1107–1114.
8. Hashimoto J, Ogawa K, Kubo A, et al. Application of transmission scan-based attenuation compensation to scatter-corrected thallium-201 myocardial single-photon emission tomographic images. *Eur J Nucl Med.* 1998;25:120–127.
9. Prvulovich EM, Lonn AHR, Bomanji JB, Jarrit PH, Ell PJ. Effect of attenuation correction on myocardial thallium-201 distribution in patients with a low likelihood of coronary artery disease. *Eur J Nucl Med.* 1997;24:266–275.
10. Rosenthal MS, Cullom J, Hawkins W, Moore SC, Tsui BM, Yester M. Quantitative SPECT imaging: a review and recommendations by the Focus Committee of the Society of Nuclear Medicine Computer and Instrumentation Council. *J Nucl Med.* 1995;36:1489–1513.
11. Sorenson JA. Methods for quantitative measurement of radioactivity in vivo by whole-body counting. In: Hine GJ, Sorensen JA, eds. *Instrumentation in Nuclear Medicine.* New York, NY: Academic Press; 1974:311–348.
12. Bailey DL, Hutton BF, Walker PJ. Improved SPECT using simultaneous emission and transmission tomography. *J Nucl Med.* 1994;28:844–851.
13. Manglos SH, Jaszczak RJ, Floyd CE, Hahn LJ, Greer KL, Coleman RE. A quantitative comparison of attenuation-weighted backprojection with multiplicative and iterative postprocessing attenuation correction in SPECT. *IEEE Trans Med Imaging.* 1988;7:128–134.
14. Hudson HM, Larkin RS. Accelerated image reconstruction using ordered subsets of projection data. *IEEE Trans Med Imaging.* 1994;13:601–699.
15. Nicholson RL, Doherty M, Wilkins K, Prato FS. Paradoxical effect of the skull on attenuation correction requirements for brain SPECT [abstract]. *J Nucl Med.* 1988;29(suppl):1316P.
16. Stodilka RZ, Kemp BJ, Prato FS, Nicholson RL. Importance of bone attenuation in brain SPECT quantification. *J Nucl Med.* 1998;39:190–197.
17. Kemp BJ, Prato FS, Dean GW, Nicholson RL, Reese L. Correction for attenuation in technetium-99m-HMPAO SPECT brain imaging [published correction appears in *J Nucl Med.* 1992;33:2250]. *J Nucl Med.* 1992;33:1875–1880.
18. Rajeevan N, Zubal IG, Ramsby SQ, Zoghbi SS, Seibyl J, Innis RB. Significance of nonuniform attenuation correction in quantitative brain SPECT imaging. *J Nucl Med.* 1998;39:1719–1726.
19. Iida H, Narita Y, Kado H, et al. Effects of scatter and attenuation correction on quantitative assessment of regional cerebral blood flow with SPECT. *J Nucl Med.* 1998;39:181–189.
20. Dey D, Slomka PJ, Hahn LJ, Kloiber R. Automatic three-dimensional multimodality registration using radionuclide transmission CT attenuation maps: a phantom study. *J Nucl Med.* 1999;40:448–455.
21. Kouris K, Clarke GA, Jarritt PH, Townsend CE, Thomas SN. Physical performance evaluation of the Toshiba GCA-9300A triple-headed system. *J Nucl Med.* 1993;34:1778–1789.
22. Kramer R, Zankl M, Williams G, Drexler G. *The Calculation of Dose from External Photon Exposures Using Reference Human Phantoms and Monte Carlo Methods. Part I: The Male (Adam) and Female (Eva) Adult Mathematical Phantoms*. Muenchen, Germany: Gesellschaft fur Strahlen- und Umweltforschung (GSF); 1986. GSF-Bericht S-885.
23. International Commission on Radiation Protection (ICRP). *Recommendations of the International Commission on Radiation Protection (ICRP): Report 60.* Oxford, UK: Pergamon Press; 1990.
24. Hoffman EJ, Cutler PD, Diby WM, Mazziota JC. Three dimensional phantom to simulate cerebral blood flow and metabolic images for PET. *IEEE Trans Nucl Sci.* 1990;37:616–620.
25. Hashimoto J, Kubo A, Ogawa K, et al. Scatter and attenuation correction in technetium-99m brain SPECT. *J Nucl Med.* 1997;38:157–162.
26. Ichihara T, Ogawa K, Motomura N, Kubo A, Hashimoto S. Compton scatter compensation using the triple-energy window method for single- and dual-isotope SPECT. *J Nucl Med.* 1993;34:2216–2221.
27. Hudson HM, Larkin RS. Accelerated image reconstruction using ordered subsets of projection data. *IEEE Trans Med Imaging.* 1994;13:601–699.
28. Talaraich J, Tournoux P. *Co-Planar Stereotactic Atlas of the Human Brain*. Stuttgart, Germany: Thieme Medical; 1988.
29. Van Laere K, Vonck K, Boon P, Brans B, Vandekerckhove T, Dierckx RA. Vagus nerve stimulation in refractory epilepsy: a SPECT activation study. *J Nucl Med.* 2000;41:1145–1154.
30. Tan P, Bailey DL, Meikle SR, Eberl S, Fulton RR, Hutton BF. A scanning line source for simultaneous emission and transmission measurements in SPECT. *J Nucl Med.* 1993;34:1752–1760.
31. White DR, Widdowson EMWHQ, Dickerson JWT. The composition of body tissues. *Br J Radiol.* 1991;64:149–159.
32. Kemp BJ, Prato FS, Nicholson RL, Reese L. Transmission computed tomography imaging of the head with a SPECT system and a collimated line source. *J Nucl Med.* 1995;36:328–335.
33. Ljungberg M, King MA, Hademenos GJ, Strand SE. Comparison of four scatter correction methods using Monte Carlo simulated source distributions. *J Nucl Med.* 1994;41:143–151.
34. Ogasawara K, Hashimoto J, Ogawa K, et al. Simultaneous acquisition of iodine-123 emission and technetium-99m transmission data for quantitative brain single-photon emission tomographic imaging. *Eur J Nucl Med.* 1998;25:1537–1544.
35. Stodilka RZ, Kemp BJ, Msaki P, Prato FS, Nicholson RL. The relative contributions of scatter and attenuation corrections toward improved brain SPECT quantification. *Phys Med Biol.* 1998;43:2991–3008.
36. Dey D, Slomka PJ, Hahn LJ, Kloiber R. Comparison of ordered subsets expectation maximization and Chang's attenuation correction method in quantitative cardiac SPET: a phantom study. *Nucl Med Commun.* 1998;19:1149–1157.
37. Harris CC, Greer KL, Jaszczak RJ, Floyd CE, Fearnow C, Coleman RE. Technetium-99m attenuation coefficients in water-filled phantoms determined with gamma-cameras. *Med Phys.* 1984;11:681–685.
38. Glick SJ, King MA, Pan TS, Soares EJ. Compensation for nonuniform attenuation in SPECT brain imaging. *IEEE Trans Nucl Sci.* 1996;43:737–750.
39. Licho R, Glick SJ, Xia W, Pan TS, Penney BC, King MA. Attenuation compensation in ^{99m}Tc SPECT brain imaging: a comparison of the use of attenuation maps derived from transmission versus emission data in normal scans. *J Nucl Med.* 1999;40:456–463.
40. Kalki K, Blankespoor SC, Brown JK, et al. Myocardial perfusion imaging with a combined x-ray CT and SPECT system. *J Nucl Med.* 1997;38:1535–1540.